Extreme UV spectroscopy measurements and analysis for tungsten density studies in the WEST tokamak

R. Guirlet, C. Desgranges, J. L. Schwob, P. Mandelbaum, M. Y. Boumendjel

Extreme UV spectroscopy measurements and analysis for Tungsten density studies in the WEST tokamak

R. Guirlet[a], C. Desgranges[a], J. L. Schwob[b], P. Mandelbaum[b,c], M. Y. Boumendjel[a] and the WEST Team[1]

[a]*CEA, IRFM, F-13108 Saint Paul-lez-Durance, France*

[b]*Racah Institute of Physics, Hebrew University of Jerusalem, Israel*

[c]*Jerusalem College of Engineering, Ramat Beth Hakerem, 91035 Jerusalem, Israel*

Abstract

The VUV emission of tungsten in WEST is measured by an absolutely calibrated grazing incidence spectrometer of the Schwob-Fraenkel type which can scan the lower half of the plasma. We have analysed the detected spectral lines in the range 120-140 Å and compared their behaviour with calculations and published information. We obtained an unambiguous identification of four intense and well resolved spectral lines emitted by W^{42+}-W^{45+} close to the magnetic axis in the analysed experiments. The measured spectral line brightnesses are used to assess the Tungsten density in the emission region. In a case of a scanning line of sight, we investigate the possibility to calculate the Tungsten density profile from the angular brightness profiles. In a case of a fixed line of sight, we deduce from the measurements the core Tungsten density profile evolution during a radiative collapse.

1. Introduction

Since the decision was taken of equipping ITER with a tungsten (W) divertor [1], several tokamaks have changed the material of their plasma-facing components to solid or coated tungsten [2-7]. This has had important consequences on the operation and performances of these devices [8, 9], primarily due to the high radiation capability of Tungsten (Z=74) which is never completely ionised in tokamaks. It is thus necessary to investigate and eventually control its sources on the plasma facing components and its transport in the scrape-off layer and the confined plasma. For the latter study, one of the essential quantities is the Tungsten density distribution in the confined plasma. As no diagnostic can provide it directly, efforts have been initiated and are still going on to determine it by combining the available Tungsten-sensitive measurements, namely the soft-X ray, bolometry and VUV spectroscopy measurements [10-12].

With no or a poor spectral resolution, the soft-X ray and bolometry diagnostics do not allow to identify and distinguish the various impurities present in the plasma. Therefore they cannot be used alone to determine accurately the Tungsten density. As, in the soft-X ray and UV domains, Tungsten has the highest radiation capability of all impurities commonly found in tokamaks, a rough assumption can sometimes be made that the measurements of these diagnostics are overwhelmingly dominated by the Tungsten contribution. A more accurate way of isolating the latter is to deduce the contributions of other (mostly light) impurities from other diagnostic measurements such as charge exchange recombination spectroscopy (CXRS) [13] and subtract them from the soft-X ray or bolometry measurements.

Conversely, VUV spectrometers, thanks to their spectral resolution, allow to isolate spectral lines or groups of lines and assign them to specific impurity ions among which tungsten ions [14-17]. It is thus a very powerful technique to identify the impurities present in a plasma. However, the high spectral resolution necessary to separate spectral lines which lie densely in the VUV wavelength range is generally obtained at the expense of the wavelength interval width. Therefore, only a limited number of Tungsten lines, and thus of Tungsten ions, can be followed during a plasma discharge. Moreover, the VUV spectrometers in tokamaks are rarely calibrated in intensity (although examples can be found in [18, 19]) so that a calibration transfer has to be made using visible spectroscopy,

[1] http://west.cea.fr/WESTteam

bolometry or soft-X ray diagnostics. In general, the spectral line brightnesses extracted from the measurements can thus be related only in relative value to the density of the emitting ion. An example of absolute values of W densities deduced from absolute W line intensities can be found in [19a].

The most complete methods aiming at determining the Tungsten density distribution combine soft-X ray, bolometry and VUV spectroscopy measurements (see for example [12]). These methods must seek a consistent interpretation of independent measurements, a rich source of knowledge about the plasma behaviour but also the reason of the greater complexity of the methods and of an increased analysis time.

The Tore Supra and WEST tokamaks have been equipped with an extreme UV (EUV), grazing incidence spectrometer (GIS) [20] called SIR which has been continuously upgraded for over three decades. Its mobile line of sight allows to scan the plasma's lower half during a discharge. In this article we investigate the possiblity to determine the density profile of several Tungsten ionisation stages using the SIR measurements independently from soft-X ray and bolometry measurements.

Section 2 describes the spectrometer features which were of use for the work presented in the next sections. Section 3 shows how the scanning capability of the SIR was used to help in the line assignment method and its results for the wavelength interval chosen for our study. Section 4 describes the emission modelling method we developed to predict the emission rate distribution of given spectral lines. Section 5 shows with examples how this model is used to interpret the grazing incidence spectrometer measurements to provide information on the core Tungsten density distribution in WEST plasmas. Section 6 summarises the results and proposes directions to develop and improve the method.

2. Grazing incidence spectrometer

The measurements analysed in this study are all performed with our EUV spectrometer of the Schwob-Fraenkel type [20] called SIR. It is equipped with two detection channels, both placed on the Rowland circle and referred to as 'short wavelength' (SW) and 'long wavelength' (LW). Since the original pblication cited above, several changes and improvements have been made over the years of which the main ones are the following:

- The detection efficiency has been enhanced by the use of double multichannel plates (MCPs) for either channel instead of single ones, each MCP being supplied with 1300 V, with almost no loss of spectral resolution with respect to a single MCP,
- A conductance limiter in the form of a narrow, deep (in the optical axis direction) slit has been added in front of the entrance slit – it allows to protect the spectrometer vacuum chamber, and in particular the MCPs, from sudden pressure rises and to suppression residual stray light at very low wavelengths,
- The final photon detection is performed by CCD cameras, one for each channel, with 1340 pixels in the wavelength direction and binned in the perpendicular direction to enhance the signal and thus improve the time resolution.

With its routinely used 600 grooves/mm grating, the spectrometer can be operated between 15 Å and 340 Å. A 300 g/mm grating has also been used occasionally in the 2016-2020 experimental campaigns to investigate the spectrum up to 680 Å. The price to pay for the high spectral resolution of the instrument (FWHM of instrument function with the 600 g/mm grating: 0.18 Å at 25 Å and 0.23 Å at 120 Å) is the somewhat narrow wavelength interval measurable during a plasma discharge : each of the two detector assemblies mobile along the Rowland circle views an interval of 23 Å (at the lowest end of the wavelength range) to 60 Å (at the highest end). The typical time resolution (i.e. the best compromise between time reolution and a satisfactory signal-to-noise ratio) is 15 ms.

The absolute brightness calibration has been performed in the lab with a Manson source [21] emitting Kα lines of six different elements in the lower wavelength part of the spectrometer domain, and a relative calibration of the domain above 113 Å has been done using spectral line brightness ratios

(branching ratios whenever possible) measured during an experimental campaign and compared with collisional-radiative calculations [18].

The spectrometer is attached to a mobile supporting frame connected to a step motor. The spectrometer thus remotely controlled can be moved periodically up and down with a typical period of 4 s, which allows to perform measurements of EUV spectra over the lower half of the plasma during stationary discharges as will be disccsued in Fig. 6 (see also [22]).

3. Line identification in the WEST spectrum

The assignment of observed spectral lines to the corresponding transition of their emitting ion is a task which is in general arduous in metallic (and especially Tungsten) environment tokamaks because of the large number of lines [23, 24] and, in the case of Tungsten, of the existence of quasi-continua [25, 26], due to so-called Unresolved Transition Arrays (UTA), which are broad (many angströms) features made of hundreds or thousands of very close, unresolved spectral lines. An example of a spectrum measured on WEST is shown in Fig. 1.

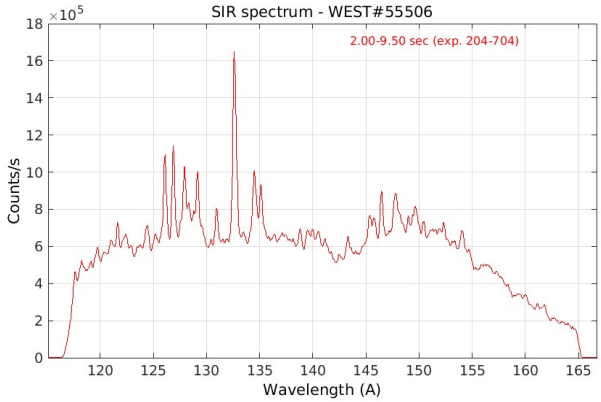

Figure 1: *Spectrum measured with the grazing incidence spectrometer during pulse WEST#55506, averaged between 2 and 9.5 s.*

A meticulous analysis of specific portions of the observed spectrum allowed us to build a list of spectral lines which can consistently be assigned to specific Tungsten ions in a broad range of plasma scenarios. In this list, the observed wavelength was obtained using a parametric wavelength calibration function valid for all possible detector positions and wavelength range. This calibration gives an accuracy of about 0.3 Å in the 110 to 150 Å wavelength interval, sufficient to unambiguously identify the lines although it gives a systematic shift of about 0.15 Å (with the used parameter values) with respect to the previously published wavelengths. In the following the measured wavelengths of [27] are adopted. To discriminate the investigated lines from lines emitted by other impurities, their brightnesses were compared with the time evolution of the pulses (particularly the electron temperature profile), the status of the wall, the plasma facing component materials etc. In the range shown in Fig. 1, about 50 spectral lines could be identified in the spectrum and assigned to the emitting ion and transition. Among them, 14 lines (shown in Table 1) are identified as emitted by W^{28+} to W^{50+} ions in the wavelength interval shown in Fig. 1.

Table 1: *list of observed spectral lines assigned to Tungsten ions in the interval shown in Fig. 1, with their measured wavelength in Å, corresponding emitting ion and initial and final levels. The strongest lines are in bold, those used in the rest of the article are marked with a* •.

Present measured wavelength (Å)	Emitting ion	Lower level	Upper level	Previous measured wavelength (Å)	Reference
121.6	W^{44+}	$4s^2\ ^1S_0$	$4s4p\ ^1P_1$	60.931 x 2	28
124.4	W^{45+}	$4s\ ^2S_{1/2}$	$4p\ ^2P_{3/2}$	62.335 x 2	28
• 126.1	**W^{43+}**	**$4s^24p\ ^2P_{1/2}$**	**$4s^24p\ ^2P_{3/2}$**	**126.29** **126.39**	27 16
• 126.8	**W^{45+}**	**$4s\ ^2S_{1/2}$**	**$4p\ ^2P_{1/2}$**	**127.12** **127.20**	27 16
127.9	**W^{43+}**	**$4s^24p\ ^2P_{1/2}$**	**$4s4p^2\ ^4P_{1/2}$**	**128.17** **128.24**	27 16
• 129.2	**W^{42+}**	**$4s^24p^2\ ^3P_0$**	**$4s^24p^2\ ^1D_2$**	**129.41** **129.45**	27 16
131.0	**W^{41+}**	**$4s^24p^3\ ^2D_{3/2}$**	**$4s^24p^3\ ^2D_{5/2}$**	**131.24** **131.21**	27 16
• 132.6	**W^{44+}** **(blended)**	**$4s^2\ ^1S_0$**	**$4s\ 4p\ ^3P_1$**	**132.88** **132.87**	27 16
134.5	**W^{39+}** **W^{40+}** **W^{42+}** **W^{43+}** **W^{44+}**	**$4s^24p^5\ ^2P_{3/2}$** **$4s^24p^4\ ^3P_2$** **$4s^24p^2\ ^1D_2$** **$4s^24p\ ^2P_{3/2}$** **$4s4p\ ^3P_1$**	**$4s^24p^5\ ^2P_{1/2}$** **$4s^24p^4\ ^3P_1$** **$4s4p^3\ ^3P_2$** **$4s4p^2\ ^2D_{5/2}$** **$4s4p\ ^3P_2$**	**134.74** **134.87** **134.88** **134.75** **134.95** **134.81** **134.80**	27 16 27 16 27 27 27
135.1	W^{42+} W^{43+}	$4s^24p^2\ ^3P_0$ $4s^24p_{3/2}\ ^2P_{3/2}$	$4s^24p^2\ ^3P_1$ $4s4p^2\ ^2D_{5/2}$	135.45 135.34	27 16
138.8	W^{41+}	$4s^24p^3\ ^2D_{3/2}$	$4s^24p^3\ ^4S_{3/2}$	138.96 139.14	16 27
146.5	W^{28+}	$4d^{10}\ ^1S_0$	$4d^94f\ ^1P_1$	48.948 x 3	29
147.7	W^{27+}	$4d^{10}4f\ ^2F_{5/2}$ $4d^{10}4f\ ^2F_{7/2}$	$4d^94f(^1P)4f\ ^2D_{3/2}$ $4d^94f(^1P)4f\ ^2D_{5/2}$	49.403 x 3	30
153.1	W^{50+} W^{49+}	$3d^4{}_{3/2}3d^2{}_{5/2}(0,4)$ [4] $3d^4{}_{3/2}3d^3{}_{5/2}(0,9/2)$ [9/2]	$3d^3{}_{3/2}3d^3{}_{5/2}(3/2,3/2)$ [3] $3d^3{}_{3/2}3d^4{}_{5/2}(3/2,4)$ [11/2]	153.63 153.68	31

For the pulse analysed in Section 5 (WEST#55506), seven lines (marked in bold blue in Table 1) were found to be of sufficient intensity to be used in our analysis. As the 134.5 Å is a blending of lines from W^{39+} to W^{44+}, its interpretation is subject to large uncertainties. Therefore it was discarded from our analysis.

On the same experimental day, we performed a discharge (WEST#55518) with the spectrometer in scanning mode with a 4 s period. As it was 40 s long and very stationary, we could investigate the brightness profiles of the spectral lines of interest to reveal some extremely useful information: the differences in position and width of the maximum brightness of various lines allow to distinguish between ions with different ionisation potentials. The time evolution of the six selected line brightnesses averaged over six periods of the scan are shown in Fig. 2 along with the line of sight angle.

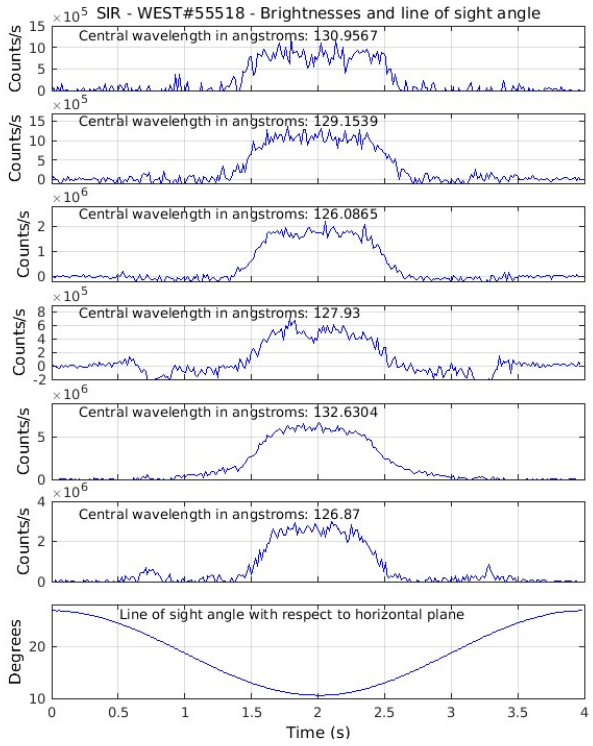

Figure 2: (a-f) Time evolution of six line brightnesses measured by the SIR spectrometer, averaged over 6 periods of the spectrometer scanning period. The time origin is arbitrarily chosen as the time of the largest angle (i.e. lowest line of sight); g) corresponding time evolution of the line of sight angle.

We exclude the line shown in Fig. 2a (tentatively assigned to W XLII) because it is rather weak and noisy around its maximum. The line brightness shown in Fig. 2d (127.93 Å, tentatively W XLIV) shows negative values for angles between 20° and 23.5°, corresponding to a line of sight outside the confined plasma ending on the outer divertor target plate. This is an indication that the W XLIV line is affected by a close line emitted in the plasma periphery with a weaker but substantial intensity. Therefore we will exclude it from the analysis. Fig. 2e shows a brightness profile with fairly broad wings extending to 18°. This is thought to be due to the blending of the W XLV line with possibly Fe XX 132.85 Å ($2s^2 2p^3\ ^4S_{3/2} - 2s2p^4\ ^4P_{5/2}$) and Fe XXIII 132.91 Å ($1s^2 2s^2\ ^1S_0 - 1s^2 2s2p\ ^1P_1$). As their contribution seems weak, we keep this line in our analysis, keeping in mind that it can lead to an overestimate of the Tungsten density. The spectral lines thus retained for the more refined analysis presented below are:

- 129.41 Å identified as W XLIII,
- 126.29 Å identified as W XLIV,
- 132.88 Å identified as W XLV,
- 127.12 Å identified as W XLVI.

Their brightness profiles (normalised to their maximum) as a function of the line of sight angle are shown in Fig. 3. The 127.12 Å line exhibits a profile substantially narrower than the other three lines and the 129.4 Å a profile substantially broader. This indicates that the former is emitted by a more central (i.e. more ionised) ion and the latter by a less central (i.e. less ionised) ion than the others, an observation in agreement with our line identification. The other two lines exhibit widths inbetween and similar to each other, consistent with our assignment of those lines to W XLIV and W XLV.

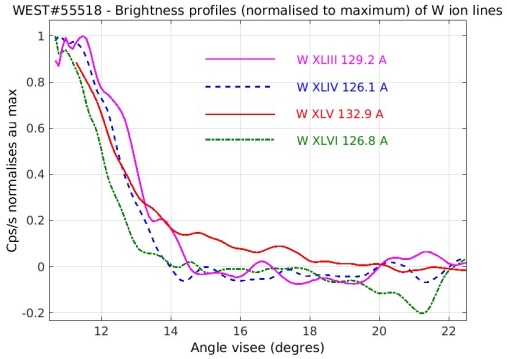

Figure 3: normalised brightness of the four selected spectral lines as a function of the line of sight angle.

4. Emission modelling

The brightness profiles, normalised in Fig. 3, are actually measured in absolute units (photons/(m^2 s sr)) thanks to the spectrometer calibration (see Section 2). It is thus possible to relate these profiles with the Tungsten density profile. Nevertheless, the relation is not a straightforward one because the measurements are integrated along a line of sight. Moreover, the photon emission is a function of the electron density and of an atomic physics coefficient. We have thus built an emission model similar to that described in [11, 12]. It computes the radial distribution of the emission from the electron density and temperature measurements and from the appropriate atomic physics coefficients.

The structure of the model is drawn from the expression relating the emissivity of a given spectral line with the density of its emitting ion:

$$\varepsilon_{Z,z}^{ij}(\rho) = n_e(\rho) n_{Z,z}(\rho) PEC_{Z,z}^{ij}\left(n_e(\rho), T_e(\rho)\right) = n_e(\rho) n_Z(\rho) f_{Z,z}(\rho) PEC_{Z,z}^{ij}\left(n_e(\rho), T_e(\rho)\right) \quad (1)$$

where n_e and T_e are the electron density and temperature, $\varepsilon_{Z,z}^{ij}$ is the emissivity (in photons/(m^{3}s^1)) of the spectral line due to a transition between energy levels i and j of an ion of charge z of an element of atomic number Z, and $PEC_{Z,z}^{ij}$ is the corresponding photon emission coefficient (PEC, in m^3/s). It is assumed throughout the article that all quantities are poloidally symmetric. This assumption is well adapted to the core of WEST plasmas as the centrifugal force is weak in WEST (there is no NBI so no direct momentum injection and the toroidal rotation induced by ICRH is at most of a few tens of kilometers per second). Moreover, the spectrometer is in a midplane port. Therefore, it integrates the emission of both the low field side and the high field side, thus averaging over a possible asymmetry.

In the right hand side of Eq. (1) we have replaced the emitting ion density $n_{Z,z}$with its expression as a function of the total density n_Z of the impurity of interest, using the so-called fractional abundance $f_{Z,z} = n_{Z,z}/n_Z$. The (generally weak) dependence of the $f_{Z,z}$ quantities on transport is neglected in the following, so that the $f_{Z,z}$ values are calculated from a local ionisation balance model. The ionisation and recombination rate coefficients used for the present calculation originate from ADAS [32] datasets containing the ADPAK data modified to match the AUG experimental findings (see Ref. [16]). All quantities in the right hand side of Eq. (1) are functions of the radial coordinate ρ, either directly ($n_{Z,z}$, n_e and T_e) or, for $PEC_{Z,z}^{ij}$, through a dependence on n_e and T_e.

When we compute a spectral line emissivity, we use Eq. (1) with the measured radial distributions of the electron density and temperature. For the PEC of the measured spectral lines selected in Section 3, we use those from the results of [27] provided in ADAS. The only remaining unknown quantity in this model is the radial density distribution of the impurity under study.

Let us first assume the impurity density is uniform in the radial direction. The radial distribution shape of the emissivity $\varepsilon_{Z,z}^{ij}(\rho)$ is then determined by the product $n_e(\rho)f_{Z,z}(\rho)PEC_{Z,z}^{ij}\left(n_e(\rho),T_e(\rho)\right)$.

As an example, we have made the calculation of this quantity first for the reference discharge (WEST#55518) with the spectrometer in scanning mode during about 40 s of stationary plasma, i.e. approximately nine periods of oscillation. The electron density and temperature profiles (deduced from interferometry and electron cyclotron emission measurements resp.) are shown in Fig. 4. The superimposition of many profiles over a time interval of several seconds shows how stationary the plasma parameters are.

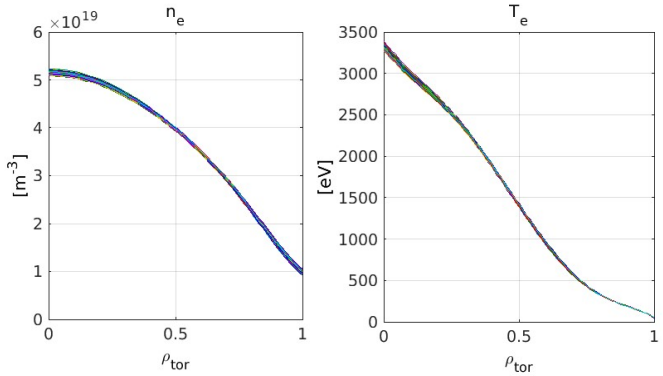

Figure 4: Radial profiles of the electron density (left) and temperature (right) as a function of the normalised radial coordinate for discharge WEST#55518. All measurements over a time range of 5 seconds are superimposed.

The radial profiles of the fractional abundances and the PECs corresponding to the selected Tungsten lines are then calculated. The results for W^{42+} 129.41 Å and W^{45+} 127. 12 Å are shown in Fig. 5.

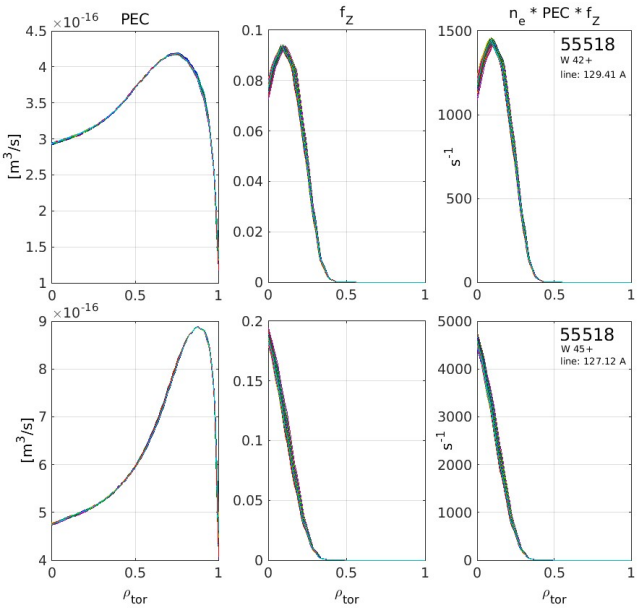

Figure 5: Radial profiles of the PEC *(left)*, of the fractional abundance *(middle)* and of the corresponding product $n_e(\rho)f_{Z,z}(\rho)PEC_{Z,z}^{ij}\left(n_e(\rho),T_e(\rho)\right)$ *(right)* for spectral lines W^{42+} 129.41 Å *(top)* and W^{45+} 127.12 Å *(bottom)*.

It can be seen that in this case the radial distribution of the line emissivities is strongly weighted by the fractional abundance of the emitting ions because the radial variation of the latter dominates largely

over those of the PECs and of the electron density. As a consequence, the radial range over which the selected spectral lines provides information is restricted to $\rho \leq 0.4$ approximately in this case.

Then, keeping the working assumption of a flat n_W profile, we have integrated the product $n_e(\rho) f_{Z,z}(\rho) PEC_{Z,z}^{ij}\left(n_e(\rho), T_e(\rho)\right)$ over lines of sight covering the core region of the plasma (see Fig. 6), as a proxy to the measured brightness profiles. The results normalised to their maximums are shown for the selected lines in Fig. 7.

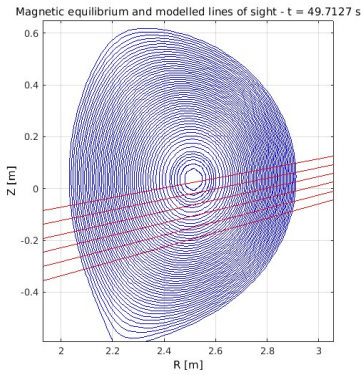

Figure 6: Magnetic equilibrium of the stationary discharge WEST#55518 and a few modelled lines of sight with angles between 10.5° and 15.5°.

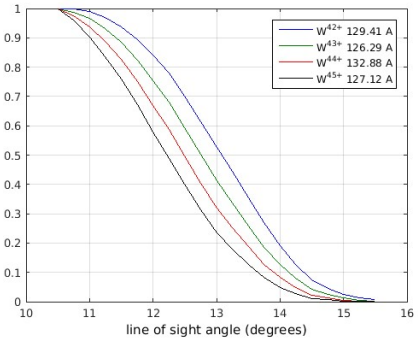

Figure 7: Modelled integral of the product $n_e(\rho) f_{Z,z}(\rho) PEC_{Z,z}^{ij}\left(n_e(\rho), T_e(\rho)\right)$ for the selected lines, normalised to their maximum as a function of the line of sight angle.

Figure 7 shows that the modelled lines emitted by ions W^{42+} to W^{45+}, although all peaked at the magentic axis, exhibit substantially different radial distributions even with a flat Tungsten density distribution. This justifies *a posteriori* the line assignment method described in Section 3.

The last step of our model is the line brightness calculation. The brightness $B_{Z,z}^{ij}$ measured by a spectrometer is proportional to the integral of the emissivity of a spectral line $\varepsilon_{Z,z}^{ij}(\rho)$ along its line of sight. With the assumption of a small radial gradient of $n_Z(\rho)$ it can be written:

$$B_{Z,z}^{ij} = \frac{1}{4\pi} \bar{n}_Z \int n_e(l) f_{Z,z}(l) PEC_{Z,z}^{ij}\left(n_e(l), T_e(l)\right) dl \qquad (2)$$

where l is the coordinate along the line of sight over which the integral is performed. Here we have replaced the impurity density $n_Z(l)$ with its average value $\bar{n}_Z$ over the path where the integrand is finite.

As neither $n_Z(\rho)$ nor $\bar{n}_Z$ are known, we can either adjust them so that the modelled $B_{Z,z}^{ij}$ matches the measured one, or compute an experimental value $\bar{n}_Z^{exp}$:

$$\bar{n}_Z^{exp} = \frac{4\pi B_{Z,z}^{ij}}{\int n_e(l) f_{Z,z}(l) PEC_{Z,z}^{ij}(n_e(l), T_e(l))\, dl} \quad (3)$$

of the impurity density from the expression above, replacing $B_{Z,z}^{ij}$ with the measured brightness and using the measured electron density and temperature and the experimental magnetic equilibrium to calculate the denominator. Because the emissivity is localised in a limited radial range determined by $n_e(\rho) f_{Z,z}(\rho) PEC_{Z,z}^{ij}\big(n_e(\rho), T_e(\rho)\big)$, $\bar{n}_Z^{exp}$ is approximately the average density of the studied impurity over this range. By combining the analysis of lines emitted by various ionisation stages of a given impurity, we can gain some information on the radial density distribution of the impurity if the ionisation stages are radially apart from each other. Alternatively, if the chosen ionisation stages are radially close we can check the consistence of the method and of the atomic data. The next Section gives two example of applications of this method to determine the W density profiles in WEST plasmas.

5. Applications

5.1. Tungsten density profile deduced from measured brightness profiles

The method described in the previous section was applied to a case with the spectrometer in scanning mode already used in Section 3 (pulse WEST#55518). We have compared the measured brightness profiles of the four selected Tungsten spectral lines with the integral of the modelled product $n_e(\rho) f_{Z,z}(\rho) PEC_{Z,z}^{ij}\big(n_e(\rho), T_e(\rho)\big)$ along a corresponding set of lines of sight. The comparison between our proxy (thin line) and the measured brightness profiles (thick line) is shown in Fig. 8. The modelled shape is very similar to the measured one: a mildly peaked, monotonously decreasing bell-shaped curve with a width at half maximum slightly above 12°. To know whether this similarity is indeed a reliable indication of a flat Tungsten density profile, we have run the model with the peaked profile shown in Fig. 9. The results are shown with a thin line and + in Fig. 8. The peaked Tungsten profile matches the measurements slightly better than the flat Tungsten profile assumption for the W^{42+} and W^{43+} lines while the difference for the W^{44+} and W^{45+} lines is very small, possibly because these ions are very close to the magnetic axis and thus weakly sensitive to a density gradient further out.

Hollow tungsten density profiles have also been tried. They do not show a significantly better agreement with the measurements. The reason why the brightness profiles of all the selected lines are fairly insensitive to the W density profile shape is most likely that the emisisivity profiles are fairly broad, and the integration along the spectrometer line of sight has an additional smoothing effect. Another way of getting information on the radial dependence of the W density is to combine information extracted from various ionisation stages. This is discussed in the next Subsection.

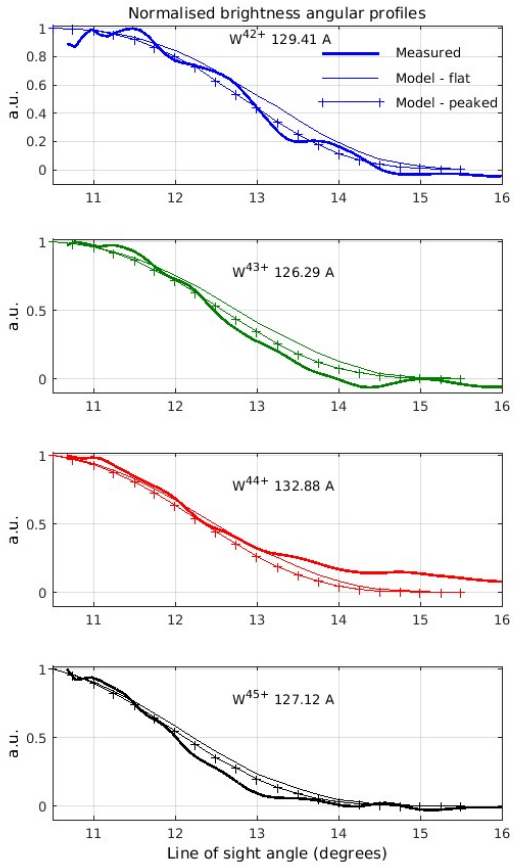

Figure 8: Angular profiles of the measured brightnesses (thick lines) and modelled brightness proxy (flat n_W profile: thin line, peaked n_W profile: thin line with +), all normalised to their maximum.

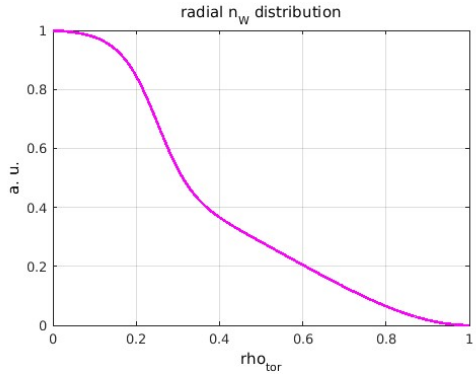

Fig. 9: peaked Tungsten density profile used in the model to compare with a flat profile (see text and Fig. 8)

5.2. Tungsten accumulation and temperature collapse

In the previous example we showed that the scanning capability of the spectrometer does not provide enough information on the Tungsten density profile shape. We will now discuss the possibility offered by measurements of spectral lines emitted by several ionisation stages when the spectrometer

is used with a fixed, central line of sight, which is the setup used in most experiments. As the spectrometer is absolutely calibrated, the method of Section 4 can be used in such cases to extract an estimate of the Tungsten density in the central part of the plasma. As an example, we chose to study a pulse of the same series as that of Section 5.1 (pulse WEST#55506). This pulse starts with ohmic heating only, then it is heated by lower hybrid wave (LH) and finally ion cyclotron resonance heating (ICRH) is added in a minority scheme, central heating scenario. The time traces of the plasma parameters are shown in Fig. 10. As can be seen the central electron temperature drops from 3.5 keV to 1.5 keV shortly after ICRH has reached the requested power. This temperature drop is accompanied with an MHD activity which may affect the tungsten distribution. The temperature then recovers for a short time before dropping again for good. The discharge ends up with a disruption.

The reason why the temperature drops during ICRH was investigated. The rise of the W^{41+} 131.24 Å line brightness (and other Tungsten lines not shown in the figure) as measured by the grazing incidence EUV spectrometer suggests a strong increase of the Tungsten density in the plasma core. As the electron density and temperature change only marginally during this rise, it can be inferred that the density of the emitting ions increases by approximately the same factor as the measured brightness, i.e. a factor 2.5-3.

The spectral interval observed with the SIR is the same as in the previous application, and thus we work with the same spectral lines. We have modelled the radius- and time-dependent product $n_e(\rho)f_{Z,z}(\rho)PEC_{Z,z}^{ij}\left(n_e(\rho),T_e(\rho)\right)$ for the selected lines in relative units to describe in more detail the Tungsten density behaviour in relation with the discharge evolution. The results are shown in Fig. 11.

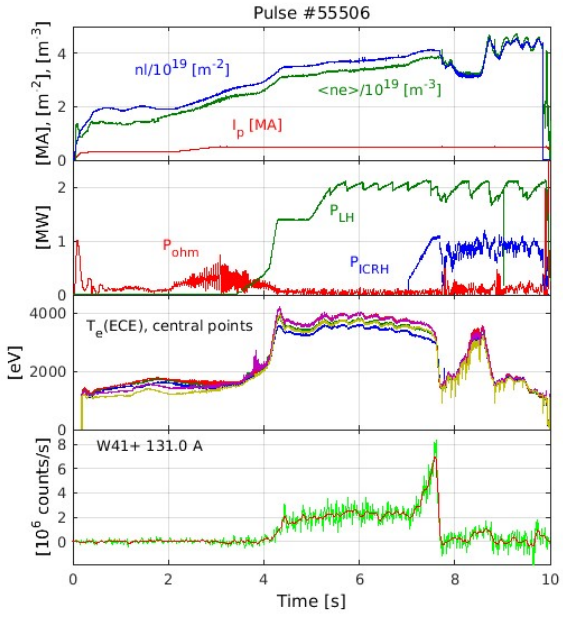

Figure 10: *Time traces of (top) the plasma current (I_p), the integrated electron density as measured by the central interferometer chord (nl) and the volume average electron density (n_e); (middle top) the ohmic power (P_{ohm}), the LH power (P_{LH}) and the ICRH power (P_{ICRH}); (middle bottom) the electron temperature as measured by the five most central ECE points; (bottom) the W^{42+} 129.41 Å line brightness in arbitrary units.*

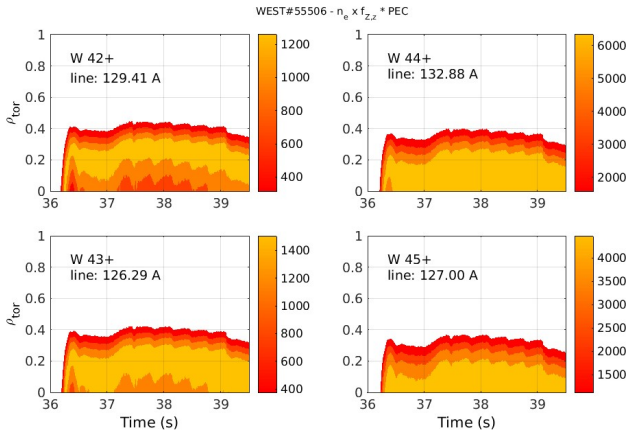

Figure 11: $n_e(\rho) f_{Z,z}(\rho) PEC_{Z,z}^{ij}\left(n_e(\rho), T_e(\rho)\right)$ as a function of time and radial coordinate for the selected Tungsten lines. Solid line: position of the maximum, dashed lines: interval comprising 70% of the radial integral. The color scale is in units [s^{-1}].

It can be seen on Fig. 11 that the radial width of the emitting layer of each line is of the order of $\Delta\rho$ = 0.2 to 0.3. It is possible that the Tungsten density is not uniform over such a fairly broad layer. Nevertheless, we have retained the assumption that the Tungsten density is uniform over each emitting layer. The average Tungsten density over the emitting layer of each spectral line is obtained by using Eq. (3), the integral being calculated over the spectrometer line of sight. The calculation has been performed for a few time points before and during the temperature drop. Later, the selected spectral lines are too weak to be analysed due to the temperature drop resulting in very low fractional abundances of W^{42+} to W^{45+}. The time evolution of the Tungsten density deduced from each line is shown in Fig. 12.

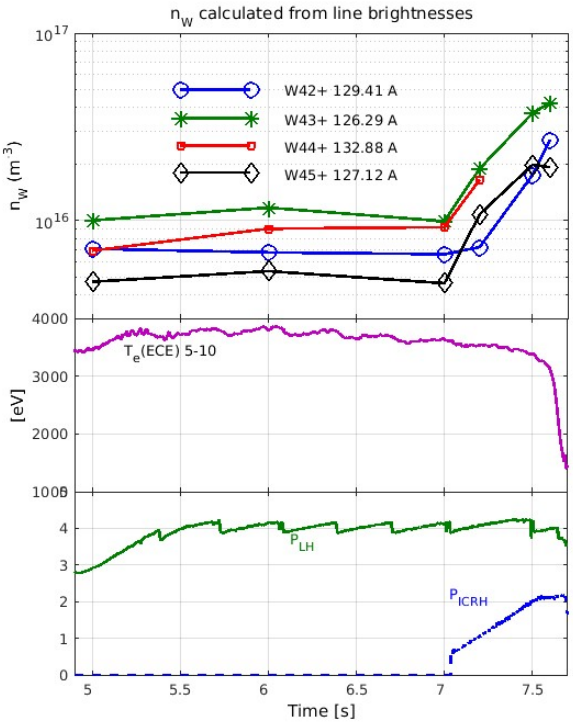

Figure 12: Time evolution of the Tungsten density (top) deduced from the selected spectral lines, of the central temperature (middle) and of the additional power (bottom) during pulse WEST#55506. The W^{44+} 132.88 Å line is saturated from t = 7.3 s.

The global trend shown in Fig. 12 is the same for all curves: the Tungsten density is stationary until 7 s, then it increases by a factor 4 approximately from 7 s. It can be seen that the Tungsten density starts to increase just after the ICRH power onset and prior to the temperature drop. It can be deduced that ICRH is the cause of the central Tungsten density rise (either due to a source effect or a transport effect), which itself is the cause of the temperature drop.

It can be seen also that the Tungsten densities deduced from the various lines differ from each other by a factor about 2. As the spectral lines have slightly different radial positions, we have used the information illustrated in Figs. 11 and 12 to build the central Tungsten density profiles as shown in Fig. 13. (we remind that the Tungsten density deduced from the W^{44+} line may be slightly overestimated, as explained in Section 3).

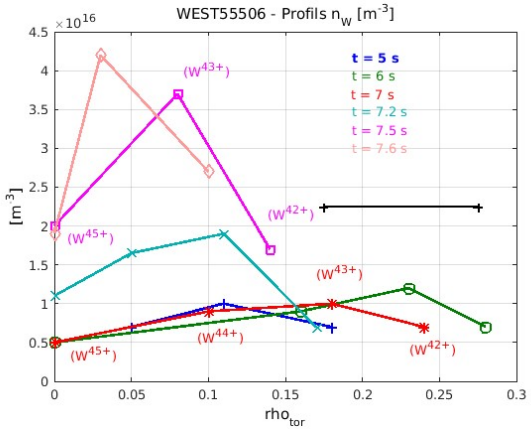

Figure 13: Tungsten density profiles deduced from the line brightnesses and the model before and during the ICRH onset. The horizontal line shows the approximate radial width over which each density point is averaged. In round brackets, the ion from which the Tungsten density value has been obtained.

From t = 5 s to t = 6 s, the LH power increases from 2.9 MW to 4 MW and the central temperature from 3.45 keV to 3.8 keV. The observed ionisation stages thus move away from the magnetic axis (from profile in blue to that in green) but the overall Tungsten density does not change and the profile remains weakly peaked until ICRH is switched on. From t = 7.2 s to 7.6 s, the global Tungsten density increases by a factor 3 to 4 and the profile becomes more and more peaked. The maximum appears to move closer to the magnetic axis, but the lack of information on W^{44+} (due to the saturation of the spectral line) makes it difficult to be quantitative. It seems however that the Tungsten density stops increasing earlier at the centre than off the axis. Note that the W^{45+} is always lower than those of W^{44+} and W^{43+} although it has the same time trend. This might indicate that the value deduced from the W^{45+} line is not consistent with to those deduced from the W^{44+} and W^{43+} lines.

In summary, the ICRH power is followed by a peaking of the Tungsten density profile within a region within approximately $\rho_{tor} = 0.15$. On the axis, the Tungsten density increases by a factor 4 but stabilises earlier than in the region $0.02 \leq \rho_{tor} \leq 0.12$ where it reaches 8 times its pre-ICRH value. The peaking and its time scale, together with the fact that the Tungsten density increases by only a factor of 2 at $\rho \approx 0.15$ are consistent with a transport effect, although a combination with an edge source effect of ICRH cannot be excluded.

6. Summary and future work

The grazing incidence EUV spectrometer operated on the WEST tokamak, with its scanning capability and its absolute calibration, is an essential diagnostic to gain knowledge on Tungsten behaviour. Our model is consistent with the identification of a set of four strong, persistent spectral lines in the 120-135 Å emitted at temperatures above approximately 2 keV as pertaining to W^{42+} to W^{45+}.

A model assuming a uniform Tungsten density within the emitting region of each of these lines separately has been developed to deduce the local Tungsten density from the line brightness measurements. It has been applied to a stationary, LH-heated pulse with the spectrometer line of sight scanning the lower half of the plasma. In the absence of the soft-X ray and bolometry diagnostics, the model combined with the line brightness measurements allows to infer that the Tungsten density profile is peaked but with very limited accuracy.

The same model has been applied to a discharge heated by LH and ICRH with a fixed line of sight of the spectrometer. Following the ICRH onset, the Tungsten density profile is shown to become more and more peaked slightly off-axis on a time scale consistent with transport. The Tungsten density within $\rho_{tor} = 0.1$ is around 7×10^{15} m^{-3} ($n_W/\langle n_e\rangle \approx 2\times10^{-4}$) and increases by a factor around 8 when ICRH is switched on. This is likely to cause the subsequent temperature drop from 3.8 keV down to 1.5 keV.

Due to the fairly high charge of the ions emitting the selected lines, the results provide information on the core region of plasmas with a central temperature above 3 keV approximately. In the near future we will investigate other spectral intervals where lower ionisation stages are expected to emit reasonably strong lines. This will allow to complete the Tungsten density profiles in the gradient regions of the hotter plasmas (central T_e above 4 keV) and to provide central information in cooler plasmas (below 3.5 keV).

In preparation of the next experimental campaign, we have also installed a very high resolution grating (2400 g/mm) which will provide measurements between 10 and 80 Å. One of the goals of this upgrade is to resolve blended lines of moderate ionisation stages in this spectral range, in particular in the 40-65 Å interval where a Tungsten UTA lies.

With Tungsten density profiles extending further from the plasma centre, the comparison with soft-X ray and bolometry measurements will be more constrained and thus the possible inconsistencies more visible.

The most limiting assumption of this work is probably that of a uniform Tungsten density within each emitting layer. Using the scanning capability of the spectrometer line of sight and a tomographic inversion of the brightness measurements in poloidally symmetric situations (a most common situation in WEST as the plasma rotation is generally low enough for the centrifugal force to play an unsignificant role), we will be able to remove this assumption and obtain Tungsten density profiles with a better radial resolution.

Acknowledgements

This work has been carried out within the framework of the EUROfusion Consortium and has received funding from the Euratom research and training programme 2014-2018 and 2019-2020 under grant agreement No 633053. The views and opinions expressed herein do not necessarily reflect those of the European Commission.

References

[1] R A Pitts et al., Phys. Scr. **T138** (2009) 014001.
[2] R Neu *et al., Plasma Phys. Control. Fusion* **49** (2007) B59
[3] A Kallenbach *et al., Nucl. Fusion* **57** (2017*)* 102015
[4] X Litaudon *et al., Nucl. Fusion* **57** (2017) 102001
[5] G F Matthews *et al., Phys. Scr.* **T138 (**2009) 014029

[6] J Bucalossi et al., *Fusion Engineering and Design* **89** (2014) 907
[7] J Bucalossi et al 2021, submitted to Nucl. Fus.
[8] T Puetterich et al., *Plasma Phys. Control. Fusion* **55** (2013) 124036
[9] C Angioni et al. *Nucl. Fusion* **54** (2014) 083028
[10] R Neu et al., *Nucl. Fus.* **45** (2005) 209
[11] T Nakano et al., *J. Phys. B: At. Mol. Opt. Phys.* **48** (2015) 144023
[12] M Sertoli et al., *Plasma Phy. Control. Fusion* **57** 075004 (2015)
[13] R M McDermott et al. 2021 *Nucl. Fusion* **61** 016019
[14] M Finkenthal et al., *Physics Letters A* **127** n°5 (1988) 255-258
[15] K Asmussen et al., *Nucl. Fusion* **38** (1998) 967
[16] T Puetterich et al., *Plasma Phys. Control. Fusion* **50** (2008) 085016
[17] Y Liu et al., *Plasma and Fusion Res.* **13** (2018) 3402020
[18] R Guirlet et al., *J. Inst.* **12** (2017) P01006
[19] K Lawson et al., *J. Inst.* **4** (2009) P04013
[19a] Yang Liu et al., *Jpn. J. Appl. Phys.* **57** 106101 (2018)
[20] J L Schwob et al., *Rev. Sci. Instrum.* **58** (9) 1601 (1987)
[21] J E Manson, *Manson model 5 ultrasoft-X ray calibration source*, Austin Instruments Inc. (1985)
[22] R Guirlet et al., *J. Inst.* **14** C10036 (2019)
[23] J Clementson et al., *J. Phys. B: At. Mol. Opt. Phys.* **43** (2010) 144009
[24] T Puetterich et al., *Plasma Phys. Control. Fusion* **50** (2008) 085016
[25] Yang Liu et al., *J. Appl. Phys.* **122** 233301 (2017)
[26] I Murakami et al., *Nucl. Fusion* **55** (2015) 093016
[27] Y Ralchenko et al., *J. Phys. B: At. Mol. Opt. Phys.* **40** (2007) 3861
[28] S B Utter et al., *Can. J. Phys.* **80** 1503 (2002)
[29] J Sugar and V Kaufman, *J. Opt. Soc. B* **10** 799 (1993)
[30] J Sugar , V Kaufman and W L Rowan, *J. Opt. Soc. B* **10** 1321 (1993)
[31] Yu Ralchenko et al., *Phys. Rev. A* **83** 032517 (2011)
[32] http://www.adas.ac.uk/ for information on the Atomic Data and Analysis Structure (ADAS)